

AUTOMATED CLASSIFICATION OF MULTI-PARAMETRIC BODY MRI SERIES

Boah Kim, Tejas Sudharshan Mathai, Kimberly Helm, Ronald M. Summers

Imaging Biomarkers and Computer-Aided Diagnosis Laboratory,
Radiology and Imaging Sciences, National Institutes of Health Clinical Center, Bethesda, MD, USA

ABSTRACT

Multi-parametric MRI (mpMRI) studies are widely available in clinical practice for the diagnosis of various diseases. As the volume of mpMRI exams increases yearly, there are concomitant inaccuracies that exist within the DICOM header fields of these exams. This precludes the use of the header information for the arrangement of the different series as part of the radiologist’s hanging protocol, and clinician oversight is needed for correction. In this pilot work, we propose an automated framework to classify the type of 8 different series in mpMRI studies. We used 1,363 studies acquired by three Siemens scanners to train a DenseNet-121 model with 5-fold cross-validation. Then, we evaluated the performance of the DenseNet-121 ensemble on a held-out test set of 313 mpMRI studies. Our method achieved an average precision of 96.6%, sensitivity of 96.6%, specificity of 99.6%, and F_1 score of 96.6% for the MRI series classification task. To the best of our knowledge, we are the first to develop a method to classify the series type in mpMRI studies acquired at the level of the chest, abdomen, and pelvis. Our method has the capability for robust automation of hanging protocols in modern radiology practice.

1. INTRODUCTION

Multi-parametric MRI (mpMRI) is a widely used imaging technique to visualize the anatomy of the body including the chest, abdomen, and pelvis, and to diagnose various diseases such as prostate cancer [1] and lymphadenopathy [2]. Due to its widespread availability today, the volume of MRI exams has increased [3]. During an MRI exam, a number of different series are acquired using a combination of echo times, repetition times, radio-frequency pulses, and other parameters. Some of the sequences provide complementary information related to disease status and are used by radiologists simultaneously. At the acquisition time, relevant information related to the series is usually stored in the “Series Description” and “Protocol Name” fields of the DICOM header.

These DICOM header fields are of particular importance as logic-based rules are applied to them. These rules facilitate the arrangement of the different series in the mpMRI study in the Picture Archival and Communication Systems (PACS) viewer. This arrangement constitutes the hanging protocol for

the radiologist who reads the study. However, there are a variety of MRI scanners from different manufacturers, diverse MRI protocols employed at different institutions across the world, and subjective preferences of the MRI technologist. These factors affect the information entered into the DICOM fields. As described in previous works [4, 5, 6, 7], ~16% of the DICOM headers contain fields that have heterogeneous, inconsistent, and subjective information. Such inaccuracies impede the use of the DICOM tags for automatic series categorization [4]. Radiologists presently rearrange the series based on their preferences and read the exam. To ameliorate the radiologist oversight necessary, an automated approach to classify the MRI sequence type would be beneficial to improving their reading efficiency.

Prior works in this area have mostly focused on classifying the series type in brain MRI studies [8, 9, 10, 11, 12, 13]. Liang et al. [8] achieved near-perfect classification accuracy for brain MRI series identification. Also, the existing research targeted towards the same task in the body has focused on either the liver [6] or the prostate [7]. Zhu et al. [6] developed a 3D pyramid pooling architecture (3DPP) for abdominal MRI series classification and achieved a “strict” accuracy of 90.4% with their 3DPP InceptionV1 network. Baumgartner et al. [7] used a ResNet-18 model to classify the type of prostate MRI sequence and obtained an overall accuracy of 99.8%. To the best of our knowledge, there is no prior work on classifying the series types in chest, abdomen, and pelvis MRI studies.

In this work, we develop a framework to automatically classify the various series in mpMRI studies acquired at the level of the chest, abdomen, and pelvis. Our pipeline is able to distinguish between 8 commonly acquired series in the MRI protocol, including pre-contrast T1-weighted, post-contrast T1-weighted (arterial, portal venous, delayed), T2-weighted, fat-suppressed T2 (T2FS), Diffusion Weighted Imaging (DWI), and Apparent Diffusion Coefficient (ADC) series. We trained a DenseNet-121 model with 5-fold cross-validation on data acquired by three different Siemens scanners. Our results demonstrate the superior performance of the ensemble on a held-out test dataset. To the best of our knowledge, we propose the first model to automatically classify the 8 series types in mpMRI studies acquired at the level of the chest, abdomen, and pelvis. Our pipeline covers ~70% of the acquired series in the body MRI protocols.

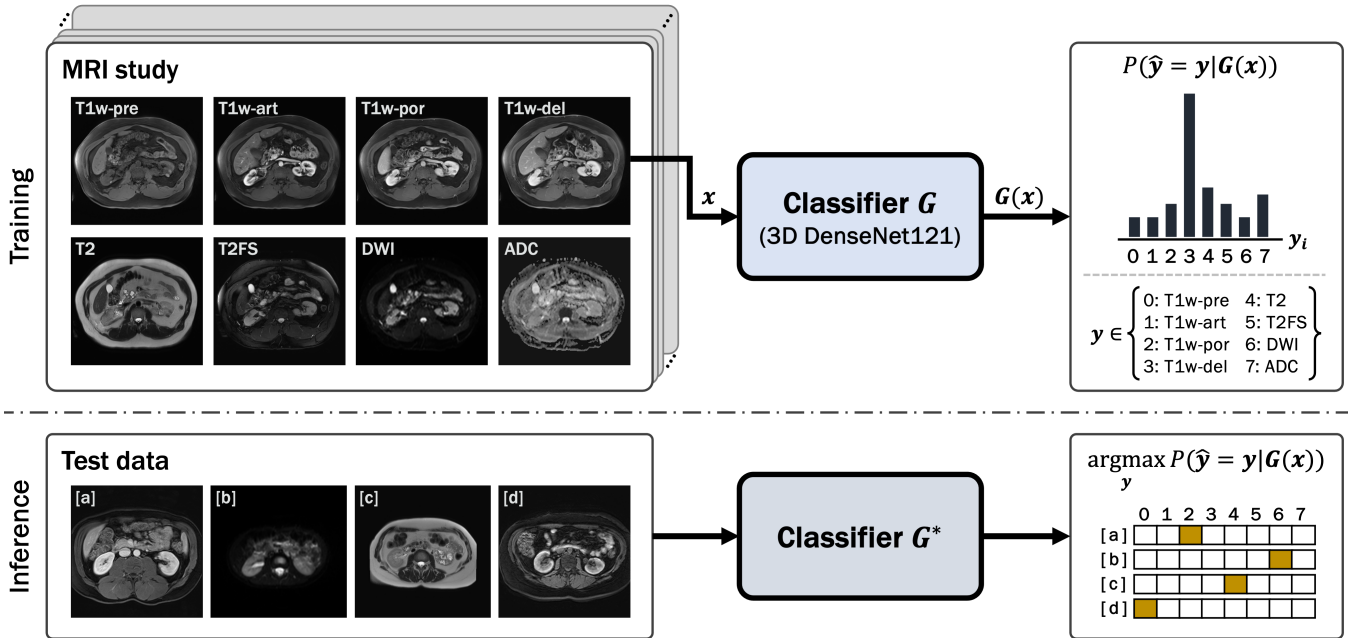


Fig. 1: The overall framework of our body mpMRI series classifier. Eight different MRI series {pre-contrast T1, T1-arterial phase, T1-venous phase, T1-delayed phase, T2-weighted, T2FS, DWI, and ADC} were used to train a 3D DenseNet-121 model with 5-fold cross-validation. At test time, the ensemble of models from each fold classified the series type of an input 3D MRI volume in the held-out test set.

2. METHODS

2.1. Data

Between January 2015 and September 2019, the PACS system at the NIH Clinical Center was queried for patients who underwent mpMRI studies of the chest, abdomen, and pelvis. A total of 2,231 studies were collected, and a majority of the patients ($n = 1399$) underwent imaging with three different Siemens scanners (Aera, Verio, and BioGraph mMR). The MRI studies for these patients were manually verified to contain all of the following 8 series: T1-weighted sequence scanned before the contrast agent injection (T1w-pre), three contrast-enhanced T1-weighted sequences in the arterial phase (T1w-art), portal venous phase (T1w-por), and delayed phase (T1w-del), T2-weighted (T2), fat-suppressed T2 (T2FS), diffusion-weighted imaging (DWI), and apparent diffusion coefficient (ADC) series that was computed from DWI. This process yielded a total of 1,676 studies from 1,216 patients. Table 1 shows a breakdown of the MRI studies based on the body part examined.

For our work, we considered only series that were acquired in the axial plane and did not include localizers, coronal, or sagittal series in the dataset. Also, based on the observation that there were often multiple DWI sequences (minimum 1, maximum 3) acquired with low ($0 - 200 \text{ s/mm}^2$), intermediate ($400 - 800 \text{ s/mm}^2$), and high ($800 - 1400 \text{ s/mm}^2$) b-values in each MRI study, we used all the available DWI

Table 1: The number of MRI studies for each body region. “Abd” denotes the abdomen region.

Region	Chest	Chest+Abd	Abd	Abd+Pelvis	Pelvis
# studies	32	1	1,573	18	52

Table 2: The number of patients and MRI studies for each fold of training, validation, and test datasets.

Fold	Train		Validation		Test	
	# patients	# studies	# patients	# studies	# patients	# studies
1	851	1202	122	161	243	313
2	852	1192	121	171	243	313
3	853	1185	120	178	243	313
4	852	1201	121	162	243	313
5	850	1199	123	164	243	313

sequences with different b-values in the studies. As shown in Table 2, the final dataset for each fold was split into training, validation, and testing sets at the patient level, such that there was no data leakage.

2.2. Model

An overview of our mpMRI classification pipeline is illustrated in Fig. 1. In the training stage, a classifier G took an MRI volume x and was trained to maximize probabilities $P(\hat{y} = y | G(x))$, where $G(x)$ is the output of the classifier, \hat{y} is the predicted sequence type, and y is the ground-truth label cor-

responding to the input. For the objective function, we employed a cross-entropy loss that can be computed by:

$$\mathcal{L}(y, \hat{y}) = - \sum_i y_i \log(\hat{y}_i). \quad (1)$$

We trained the classifier networks with five-fold cross-validation, in which for each fold, the model weights associated with the epoch achieving the highest validation accuracy were saved. In the inference stage, the classification models with the fixed learnable parameters for each fold, G^* , were ensembled together by averaging the output of probabilities. Then, the final sequence type for the input test volume was predicted via the argmax function, i.e., $\text{argmax}_y P(\hat{y} = y | G(x))$.

For implementing the classification network G , similar to prior work [10, 6], we initially adopted the ResNet-50 neural network [14] for the classification of 3D multi-parametric MRI sequences. We also compared the results of this model against the DenseNet-121 architecture [15], which previously described improved classification results over the ResNet models. These models were implemented using the Medical Open Network for Artificial Intelligence (MONAI) framework [16]. MONAI is an open-source machine-learning framework for medical imaging built on a PyTorch base.

3. EXPERIMENTS & RESULTS

3.1. Implementation details

For each MRI series volume, we resampled the data to have a consistent voxel size of $1.5 \times 1.5 \times 7.8$ mm across volumes. Also, the voxel intensities were normalized into the range of [1%, 99%] [17] to standardize the intensity distribution. Next, we resized each volume into a spatial dimension of $256 \times 256 \times 36$ through center-cropping or zero-padding. In training, we randomly rotated the volumes with 90 degrees for data augmentation.

Using a batch size of 2, the model was trained via the Adam optimization algorithm with a learning rate of .0001 for a total of 25 epochs. At inference time, we evaluated the model using the evaluation metrics of the precision, sensitivity, specificity, and F_1 scores. All experiments were conducted with the Pytorch library in Python using an NVIDIA DGX workstation running Ubuntu 20.04 LTS with a single NVIDIA A100-SXM4-40GB GPU.

3.2. Results

We trained both the ResNet-50 and DenseNet-121 classifiers on the studies acquired by the Siemens scanners ($n = 1363$) and evaluated the performance of each model on the studies acquired by the same scanner in the test data split ($n = 313$). As shown in Table 3, we observed that the DenseNet-121 model had higher metrics across the board compared to the

Table 3: Comparison of classification results by the ResNet-50 and DenseNet-121 model ensemble on the test dataset ($n = 313$ studies). Bold font indicates best results.

Model	Precision	Sensitivity	Specificity	F1 score
ResNet-50	95.86	95.86	99.53	95.85
DenseNet-121	96.60	96.59	99.62	96.59

Table 4: Breakdown of classification results for DenseNet-121 model on our test dataset ($n = 313$ studies). The total score for each metric was computed by averaging the score across all series types.

Series	Precision	Sensitivity	Specificity	F1 score
T1w-pre	99.36	99.68	99.93	99.52
T1w-art	98.01	94.25	99.79	96.09
T1w-por	87.34	88.18	98.58	87.76
T1w-del	89.66	91.37	98.83	90.51
T2	99.37	100.00	99.93	99.68
T2FS	99.68	99.36	99.96	99.52
DWI	100.00	99.89	100.00	99.95
ADC	99.37	100.00	99.93	99.68
Total	96.60	96.59	99.62	96.59

ResNet-50. The DenseNet-121 ensemble model achieved an overall average precision of 96.6%, sensitivity of 96.6%, specificity of 99.6%, and F_1 score of 96.6%. The confusion matrices for both classifiers are shown in Fig. 2. These results indicated that the ensemble of the two classifiers correctly identified 5 out of 8 series with high precision. Table 4 provides a breakdown of the metrics for the DenseNet-121 model for each series in the test data split. Although the T1 dynamic contrast-enhanced series (arterial, portal venous, and delayed phases) were confused most often with each other, the DenseNet-121 ensemble attained higher classification scores in contrast to the ResNet-50 ensemble.

4. DISCUSSION

Our DenseNet-121 model achieved superior performance over the ResNet-50 model with an average specificity of 99.6%, sensitivity of 96.6%, and F_1 score of 96.6%. It precisely classified ($\geq 95\%$) pre-contrast T1, T2-weighted, T2FS, DWI and ADC series respectively. The confusion matrix in Fig. 2 also reflects this observation with fewer misclassifications.

Despite this performance, several trends were observed. Primarily, the model had difficulty discerning between series that contained similar patterns in voxel intensity. For example, from Fig. 1, the most common error was seen when the portal venous phase of T1-weighted imaging was incorrectly labeled as the delayed phase of T1-weighted imaging, and vice-versa. Similarly, the arterial phase of T1w imaging was also confused with the portal venous phase. However, these

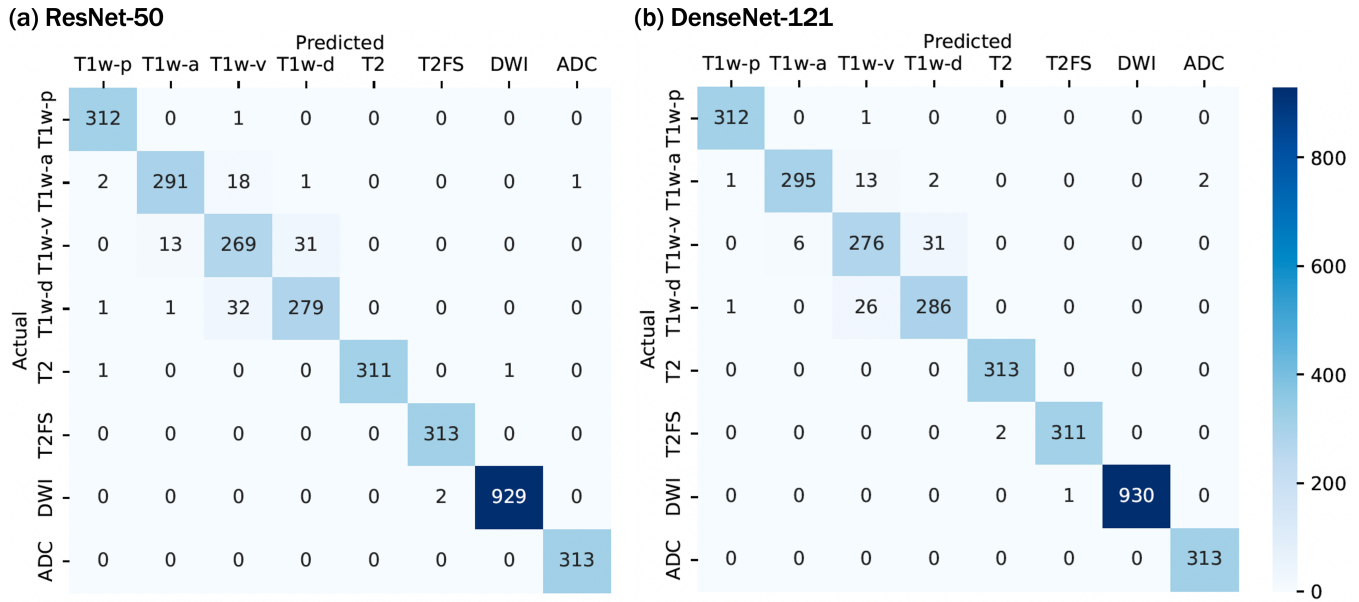


Fig. 2: Confusion matrix for our (a) ResNet-50 and (b) DenseNet-121 ensemble predictions on the test dataset ($n = 313$ studies). -p, -a, -v, and -d denote the pre-contrast, arterial, portal-venous, and delayed phase of T1-weighted imaging respectively.

types of misclassifications are considered less significant or non-significant [6] by radiologists for the clinical display of the exam. These sequences are a constituent part of the post-contrast fat-suppressed T1-weighted series (same pulse MRI series type). The only difference between them is the elapsed time post-injection of the contrast material, and there are relatively inconsistent acquisition times across different institutions around the world.

A limitation of our work is the classification of only 8 series from the MRI protocols. With the consideration of the various sequences in this work, we have attempted to cover about 70% of the MRI protocols at our institution. However, we have excluded a number of other series, such as the localizers, in-/out- phase T1w, sagittal, and coronal series in the mpMRI studies. Furthermore, depending on the anatomical region of interest, institutions around the world may have additional series that are a part of their MRI protocol. These include early arterial T1w imaging, late dynamic T1w imaging, inversion series, subtraction series etc. Some of these series fall into the same categories of series that we have chosen to classify in our work. For example: early arterial T1w series is often considered as the same series as arterial T1w, and late dynamic T1w is similar to portal-venous T1w [6].

Another limitation of our work is the sole dependence on volumetric voxel data for the automated classification of the MRI series. Currently, we do not use the wealth of information from the DICOM headers that may prove beneficial for the classification task. Furthermore, the data used in this work was acquired from only one manufacturer (Siemens) at our institution. The generalization of the model ensemble performance to studies acquired by different manufacturers (e.g.,

Philips, GE, Toshiba) remains undetermined. A remedy for this issue would be to use MRI volumes from public datasets [18] to maximize the variety of manufacturers in the training dataset.

5. ACKNOWLEDGEMENTS

This work was supported by the Intramural Research Program of the NIH Clinical Center (project number 1Z01 CL040004). Boah Kim, Tejas Sudharshan Mathai, and Kimberly Helm have no conflicts of interest. Ronald M. Summers received royalties for patents or software licenses from iCAD, Philips, ScanMed, PingAn, Translation Holdings, and MGB, and his lab received research funding through a Cooperative Research and Development Agreement from PingAn.

6. COMPLIANCE WITH ETHICAL STANDARDS

This study was approved by the Institutional Review Board (IRB) at the NIH and performed with retrospectively acquired patient data. The need for informed consent was waived.

7. REFERENCES

- [1] Baris Turkbey and Andrei S. Purysko, “Pi-rads: Where next?,” *Radiology*, vol. 307, no. 5, pp. e223128, 2023, PMID: 37097134.
- [2] Tejas Sudharshan Mathai et al., “Universal detection and segmentation of lymph nodes in multi-parametric

- mri,” *International Journal of Computer Assisted Radiology and Surgery*, vol. 1, 2023.
- [3] OECD, *Health at a Glance 2023*, 2023.
- [4] Mark Oliver Gueld et al., “Quality of DICOM header information for image categorization,” in *Medical Imaging 2002: PACS and Integrated Medical Information Systems: Design and Evaluation*, Eliot L. Siegel and H. K. Huang, Eds. International Society for Optics and Photonics, 2002, vol. 4685, pp. 280 – 287, SPIE.
- [5] Akshaya Anand et al., “Automated classification of intravenous contrast enhancement phase of ct scans using residual networks,” in *Medical Imaging 2023: Computer-Aided Diagnosis*, Khan M. Iftekharuddin and Weijie Chen, Eds. International Society for Optics and Photonics, 2023, vol. 12465, SPIE.
- [6] Zhe Zhu et al., “3d pyramid pooling network for abdominal mri series classification,” *IEEE Transactions on Pattern Analysis and Machine Intelligence*, vol. 44, no. 4, pp. 1688–1698, 2022.
- [7] Georg L. Baumgärtner et al., “Metadata-independent classification of mri sequences using convolutional neural networks: Successful application to prostate mri,” *European Journal of Radiology*, vol. 166, pp. 110964, 2023.
- [8] Shuai Liang et al., “Magnetic resonance imaging sequence identification using a metadata learning approach,” *Frontiers in Neuroinformatics*, vol. 15, 2021.
- [9] Sara Ranjbar et al., “A deep convolutional neural network for annotation of magnetic resonance imaging sequence type,” *Journal of Digital Imaging*, vol. 33, pp. 439–446, 2020.
- [10] Pablo Vieira de Mello et al., “Deep learning-based type identification of volumetric mri sequence,” *arXiv*, 2021.
- [11] Tomoyuka Noguchi et al., “Artificial intelligence using neural network architecture for radiology (ainnar): classification of mr imaging sequences,” *Japanese Journal of Radiology*, vol. 36, pp. 691–697, 2018.
- [12] Samuel Remedios et al., “Classifying magnetic resonance image modalities with convolutional neural networks,” in *Medical Imaging 2018: Computer-Aided Diagnosis*, Nicholas Petrick and Kensaku Mori, Eds. International Society for Optics and Photonics, 2018, vol. 10575, p. 105752I, SPIE.
- [13] Yiyu Chou et al., “Automatic classification of MRI contrasts using a deep Siamese network and one-shot learning,” in *Medical Imaging 2022: Image Processing*, Olivier Colliot and Ivana Išgum, Eds. International Society for Optics and Photonics, 2022, vol. 12032, p. 120320G, SPIE.
- [14] He K., and others, “Deep residual learning for image recognition,” in *IEEE Conference on Computer Vision and Pattern Recognition*, June 2016.
- [15] Gao Huang et al., “Densely connected convolutional networks,” in *Proceedings of the IEEE Conference on Computer Vision and Pattern Recognition (CVPR)*, July 2017.
- [16] Cardoso M. et al., “MONAI: An open-source framework for deep learning in healthcare,” in *arXiv*, November 2022.
- [17] Marcin Kociotek et al., “Does image normalization and intensity resolution impact texture classification?,” *Computerized Medical Imaging and Graphics*, vol. 81, pp. 101716, 2020.
- [18] Jacob A. Macdonald et al., “Duke liver dataset: A publicly available liver mri dataset with liver segmentation masks and series labels,” *Radiology: Artificial Intelligence*, vol. 5, no. 5, pp. e220275, 2023, PMID: 37293348.